



LJMU Research Online

Ren, XJ, Shi, Z, Liu, S, Gao, Y, Zhou, Y, Xing, X and Yang, Q

Mechanism of Y₂O₃ as heterogeneous nucleus of TiC in hypereutectic Fe- Cr-C-Ti-Y₂O₃ coating: first principle calculation and experiment research

<http://researchonline.ljmu.ac.uk/id/eprint/7361/>

Article

Citation (please note it is advisable to refer to the publisher's version if you intend to cite from this work)

**Ren, XJ, Shi, Z, Liu, S, Gao, Y, Zhou, Y, Xing, X and Yang, Q (2017)
Mechanism of Y₂O₃ as heterogeneous nucleus of TiC in hypereutectic Fe-Cr-C-Ti-Y₂O₃ coating: first principle calculation and experiment research.
Materials Today Communications. 13. pp. 80-91. ISSN 2352-4928**

LJMU has developed **LJMU Research Online** for users to access the research output of the University more effectively. Copyright © and Moral Rights for the papers on this site are retained by the individual authors and/or other copyright owners. Users may download and/or print one copy of any article(s) in LJMU Research Online to facilitate their private study or for non-commercial research. You may not engage in further distribution of the material or use it for any profit-making activities or any commercial gain.

The version presented here may differ from the published version or from the version of the record. Please see the repository URL above for details on accessing the published version and note that access may require a subscription.

For more information please contact researchonline@ljmu.ac.uk

<http://researchonline.ljmu.ac.uk/>

Mechanism of Y_2O_3 as heterogeneous nucleus of TiC in hypereutectic Fe-Cr-C-Ti- Y_2O_3 coating: first principle calculation and experiment research

Zhijun Shi^{a, +}, Sha Liu^{a, +}, Yukui Gao^b, Yefei Zhou^{a, c}, Xiaolei Xing^a, Xuejun Ren^d,
Qingxiang Yang^{a, *}

^a State Key Laboratory of Metastable Materials Science & Technology, Yanshan University, Qinhuangdao 066004, PR China

^b School of Aerospace Engineering and Applied Mechanics, Tongji University, Shanghai 200092, PR China

^c College of Mechanical Engineering, Yanshan University, Qinhuangdao 066004, PR China

^d School of Engineering, Liverpool John Moores University, Liverpool L3 3AF, UK

* Corresponding author: Tel. +86-335-838-7471, Fax. +86-335-807-4545

+ These authors contributed equally to this work.

E-mail address: qxyang@ysu.edu.cn, 754689046@qq.com

Abstract: The lattice misfit between Y_2O_3 and TiC low index faces was calculated by the Bramfitt two-dimensional lattice misfit theory in this work. The interface electronic structure, adhesive work and interfacial energy of Y_2O_3 (111)/TiC(110) interfaces were calculated by the first principles method. The interfacial bonding characters were analyzed by the interface charge density, electron density difference and mulliken populations. The microstructure of the hypereutectic Fe-Cr-C-Ti- Y_2O_3 coating was observed by field emission scanning electron microscopy (FESEM) and transmission electron microscopy (TEM). The calculational results show that, the lattice misfit of Y_2O_3 (111)/TiC(110) interface is 8.6%, which meets that Y_2O_3 acts as

medium effective heterogeneous nucleus of TiC. Four interface models have been constructed according to the surficial termination situations and interfacial atomic stacking modes, in which O-TiC₂ interface is most stable. Its interface adhesive work is the largest (6.07J/m²) and its interfacial energy is the smallest (-1.22J/m²). And its interfacial bonding is a mixture of polar covalent, metallic and electrovalent bonds, which proves that Y₂O₃ and TiC can form a stable interface. The experimental results show that, Y₂O₃ particle exists in the core of the flower-like TiC particle in the hypereutectic Fe-Cr-C-Ti-Y₂O₃ coating and they are combined tightly, which proves that Y₂O₃ can act as the heterogeneous nucleus of TiC.

Keywords: Y₂O₃; TiC; first principles; heterogeneous nucleation; hypereutectic Fe-Cr-C-Ti-Y₂O₃ coating

1. Introduction

With high hardness and excellent wear resistance, hypereutectic Fe-Cr-C coating has been applied in industrial remanufacturing field widely [1]. As the main strengthening phase [2], the primary M₇C₃ carbides determine the service life of the hypereutectic Fe-Cr-C coating [3]. However, they usually break and desquamate during the service process due to their coarse size, which leads to the failure of the hypereutectic Fe-Cr-C-Ti-Y₂O₃ coating [4]. Therefore, the coarse primary M₇C₃ carbides restrict the application of the hypereutectic Fe-Cr-C coating. It is significant to refine the primary M₇C₃ carbides in hypereutectic Fe-Cr-C coating to improve its service life and achieve high quality coatings without increasing cost [5].

Transition metal carbide TiC has become a research focus in the industrial and

technological applications due to its high hardness, high melting point and so on [6]. Because of the excellent performance, TiC is often used as a rigid reinforced phase in the coatings to improve their wear resistance [7]. Meanwhile, TiC particles can also play a role of heterogeneous nucleus, which refines the microstructure of the coatings and improves their mechanical performance. M. Fattahi et al. [8] revealed that TiC particles can refine the microstructure of aluminum alloy, and promote its mechanical properties obviously. K.K. Patel et al. [9] proved that TiC can refine the grains of Al-Mg alloy.

Rare earth oxides have been known as 'vitamin' of modern industry for their purification, modification and refinement effects, K. Hamano et al. [10] researched about the sintering behavior of aluminum with rare earth oxides (Y_2O_3 , La_2O_3 , Sm_2O_3 and Er_2O_3), which shows that rare earth oxides can react with impurities and purifies the molten bath. A. Noviyanto et al. [11] revealed the modification effect of rare earth oxides (Sc_2O_3 , CeO_2 , Nd_2O_3 , Sm_2O_3 , Gd_2O_3 , Dy_2O_3 , Ho_2O_3 , Er_2O_3 , La_2O_3 , Tm_2O_3 , Yb_2O_3 and Lu_2O_3), which can improve the bonding strength and contribute to achieve a dense SiC. Meanwhile, rare earth oxides also have refinement effect. Y. Chen et al. [12] researched the effect of La_2O_3 on microstructure and mechanical properties of TiC/W composite materials, which show that grains can be refined, and the hardness and elastic modulus can be improved by La_2O_3 additive simultaneously.

Our previous researches show that, when Ti additive was added in the hypereutectic Fe-Cr-C coating, TiC precipitates before the primary M_7C_3 carbides. The work of adhesion of M_7C_3 /TiC interface is 3.48 J/m^2 and the interfacial energy of

M_7C_3 /TiC interface ranges from 0.921 J/m² to 2.782 J/m². The M_7C_3 /TiC interface is theoretically stable. Therefore, TiC can be heterogeneous nucleus of the primary M_7C_3 carbides and refine them [13]. Moreover, when Y_2O_3 was added in the hypereutectic Fe-Cr-C coating, the two-dimensional lattice misfit of Y_2O_3 / M_7C_3 interface is 4.91%, which indicated that Y_2O_3 as heterogeneous nucleus of M_7C_3 carbides is middle effective, so that the primary M_7C_3 carbides can be refined [14]. On the basis of the above works, we added Ti and Y_2O_3 additives into the hypereutectic Fe-Cr-C alloy simultaneously, and found that the primary M_7C_3 carbides can be refined further. For the reasons that primary M_7C_3 was refined by TiC and Y_2O_3 together, we considered that Y_2O_3 can refine the TiC by acting as its heterogeneous nucleus, so that the number of TiC particles can be increased. Therefore, the primary M_7C_3 carbide can be further refined by the refined TiC particles. However, it is not clear about the interface relationship between TiC and Y_2O_3 , and the mechanism of TiC refined by Y_2O_3 can hardly be explained by experiment because of the tiny Y_2O_3 and TiC particles.

In recent years, first principles calculation based on density functional theory has aroused wide attention due to its feasibility in analyzing the interfacial relationships between various phases [15]. S.X. Jin et al. [16] revealed the structure, energy and electronic properties of TaN/ReB₂ interface. The results show that the Re-N₂ type interface is most stable and strong covalent bonds are formed between B and N atoms. K. Li et al. [17] delved the Mg/Al₄C₃ interface and found all interfacial energies are negative values, which are far smaller than the solid-liquid interfacial

energy of Mg ($0.1\text{J}/\text{m}^2$). The results proved that Al_4C_3 can be the heterogeneous nucleus of Mg. J. Li et al. [18] researched the $\text{Al}(001)/\text{Al}_3\text{Ti}(001)$ interfaces with different stacking modes, and concluded that the center site stacking mode is most stable from interface adhesion work and interfacial energy points. However, $\text{Y}_2\text{O}_3/\text{TiC}$ interface calculated by the first principle has not been reported.

Based on the above analysis, the Bramfitt two dimensional lattice misfit between Y_2O_3 and TiC was calculated firstly. Then, the interfacial properties of $\text{Y}_2\text{O}_3(111)/\text{TiC}(110)$ were calculated by first principle method. The interfacial stability was analyzed by interface adhesion work and interfacial energy. Meanwhile, the interface bonds were characterized by electron density difference and mulliken populations. Lastly, the possibility of Y_2O_3 as heterogeneous nucleus of TiC was analyzed. On this basis, the hypereutectic Fe-Cr-C-Ti- Y_2O_3 coating was prepared by surfacing welding and the refinement mechanism of Y_2O_3 on TiC was proved by experimental methods.

2. Calculation and experimental methods

2.1 Calculation method

In this paper, the first principle method was conducted based on the density functional theory (DFT) [19], which is implemented in the Cambridge Sequential Total Energy Package (CASTEP) module. The ultrasoft pseudopotentials were employed to represent the interactions between valence electrons and ionic core [20]. The Generalized Gradient Approximation (GGA) with the Perdew Burke Ernzerhof (PBE) function was executed as the exchange associated functions in calculations.

The models used in the computations are single unit cells of TiC bulk (1×1) and Y₂O₃ bulk (1×1). Atomic wave function cutoff energies [21] for bulk and surface calculations were set as 350eV for TiC and 340eV for Y₂O₃, while those for interface calculations were set as 340eV. K-points sampling, which plays a role of sampling in brillouin zone, was acquired by Monkhorst-Pack method [22]. K-point samplings of 8×8×8 were adopted for bulk calculations, while those of 8×5×1 were adopted for surface and interface calculations. Energy change convergence value was less than 1.0×10⁻⁵eV/atom, the largest force was 0.03eV/Å, and the maximal displacement was 1.0×10⁻³Å. The Broyden Fletcher Goldfarb Shannon (BFGS) algorithm was applied to relax the models [23] and make them reach the optimized structures [24].

2.2 Experimental method

Hypereutectic Fe-Cr-C-Ti-Y₂O₃ coating was prepared by surfacing welding method. Elemental distribution mapping of the coating was analyzed by Hitachi S3400N field emission scanning electron microscope (FESEM). The microstructure of the hypereutectic Fe-Cr-C-Ti-Y₂O₃ coating was observed by JEM-2010 transmission electron microscope (TEM).

3. Results and discussion

3.1 Lattice misfit between Y₂O₃ and TiC

The Bramfitt two-dimensional lattice misfit is calculated by Eqs. [25]:

$$d_{(hkl)_n}^{(hkl)_s} = \sum_{i=1}^3 [(|d_{[uvw]_s}^i \cos \theta - d_{[uvw]_n}^i| / d_{[uvw]_n}^i) / 3] \times 100\% \quad (1)$$

where (hkl)_s is a low-index lattice plane of nucleation substrate; (hkl)_n is a low-index lattice plane of nucleating phase; [uvw]_s is a low-index crystal orientation in (hkl)_s;

$[uvw]_n$ is a low-index crystal orientation in $(hkl)_n$; $d_{[uvw]_s}$ is the interatomic spacing along $[uvw]_s$; $d_{[uvw]_n}$ is the interatomic spacing along $[uvw]_n$; θ is the angle between the $[uvw]_s$ and $[uvw]_n$.

According to the Bramfitt two-dimensional lattice misfit theory, substrate phase can be very effective heterogeneous nucleus of nucleating phase when the lattice misfit between them is smaller than 6%; substrate phase can be medium effective heterogeneous nucleus of nucleating phase when the lattice misfit between them is in the range from 6% to 12%; and substrate phase cannot be effective heterogeneous nucleus of nucleating phase when the lattice misfit between them is larger than 12%.

Fig 1 is the crystal structures of TiC and Y_2O_3 . Fig 1(a) is the crystal structure of TiC, which is NaCl-type structure, and whose lattice parameter is 4.33Å [27]. Fig 1(b) is the crystal structure of Y_2O_3 , which is CaF_2 -type structure with disorderly oxygen vacancy, and whose lattice parameter is 5.26Å [26]. In order to make the crystal structure of Y_2O_3 accord with the atomic ratio of the actual situation, the virtual crystal approximation (VCA) method was used to modify the Y_2O_3 structure [28]. The occupancy of each Y atom in the cell is set to 1.0, which means the probability of Y atom appears in its position is 100%. And the occupancy of each O atom is set to 0.75, which means the probability of O atom appears in its position is 75%. The lattice constant of TiC after optimization is 4.33 Å, which is the same as the measurement result ($a=4.33$ Å) in Ref [27] and the calculation result ($a=4.33$ Å) in Ref [29]. The lattice constant of Y_2O_3 after optimization is 5.68 Å, which is close to the result of high temperature experiment ($a=5.26$ Å) [26].

On the basis of the lattice optimization, the lattice misfit of Y_2O_3/TiC interface was calculated, which is listed in Table 1. The lattice misfit of $Y_2O_3(111)/TiC(110)$ interface is 8.6%, within the scope of medium effective heterogeneous nucleus. So, the Y_2O_3 (111) plane and TiC (110) plane can be chosen to build surface and interface models.

Table 1 Calculated lattice misfit between Y_2O_3 and TiC

Matching face	$Y_2O_3(111)//TiC(110)$			$Y_2O_3(111)//TiC(111)$			$Y_2O_3(100)//TiC(100)$		
[uvw] Y_2O_3	[112]	[110]	[101]	[101]	[011]	[110]	[010]	[001]	[011]
[uvw] TiC	[110]	[001]	[111]	[101]	[011]	[110]	[010]	[001]	[011]
$\theta(^{\circ})$	0	0	5.264	0	0	0	0	0	0
$dY_2O_3(\text{\AA})$	6.856	3.958	7.916	3.723	3.723	3.723	5.597	5.597	7.915
$dTiC(\text{\AA})$	6.129	4.334	7.506	3.071	3.071	3.071	4.334	4.334	6.129
$\delta(\%)$	8.60%			21.20%			22.60%		

3.2 Bulk property

3.2.1 Bulk property of TiC

Fig 2 is the bulk property of TiC . Fig 2(a) is the phonon dispersion spectrum of TiC . It is obvious that there is no imaginary frequency in it, which proves the structure of TiC in this paper is stable. Fig 2(b) is the bond structure of TiC , in which a band across the Fermi level and it indicates that TiC is of metallic character. Fig 2(c) is the density of states (DOS) of TiC . The Fermi level is indicated by dashed line. The partial density of states (PDOS) of Ti and C atoms has weak peaks at Fermi level, which indicates that TiC has a certain number of metallic bonding. From -6eV to Fermi level, Ti -3d and C -2p electron orbitals resonate obviously and the DOS peaks present symmetry on both sides of the Fermi level, which suggests the formation of

covalent bonds. Furthermore, from -12.5eV to -8.8eV, Ti-3d electron orbital interacts with C-2s orbital, which also contributes to the formation of covalent bond. The above analysis illustrates that the bonding of TiC is a mixture of metallic bond and polar covalent one.

3.2.2 Bulk property of Y_2O_3

Fig 3 is the bulk property of Y_2O_3 . Fig 3(a) is the phonon dispersion of Y_2O_3 . It is obvious, there is no imaginary frequency in it, which proves the structure of Y_2O_3 in the calculation is stable. Fig 3(b) is the bond structure of Y_2O_3 , and it shows that Y_2O_3 emerges some metal characteristics. Fig 3(c) is the DOS of Y_2O_3 , and the PDOS of Y and O atoms have weak peaks at the Fermi level, which indicates that Y_2O_3 contains a certain number of metallic bonding. Within the scope of -3.7 eV to the Fermi level, Y-3d and O-2p electron orbitals are interacted. That the DOS peak intensity in Fermi level mainly owes to the contribution of O-2p orbitals, while the contribution of Y-3d is very little, which show that electrons are partial to O atoms and forming strong polarity ionic bonding. Within the scope of -16.8eV to -14.4eV, the interaction of Y-3d and O-2s orbitals also has some contribution to the formation of ionic bond. Therefore, the bond type of Y_2O_3 is a mixture of ionic bond and metallic one.

3.3 Surface convergence test

Before building the interface models, surface convergence tests of TiC and Y_2O_3 slabs were executed to determine the smallest atomic layers as well as to achieve the bulk properties. 20Å vacuum layers were added in the slabs. In order to eliminate the

effect of dipole, the terminations of the upper and lower surfaces of the slab are the same.

Fig 4 is the surface models of TiC and Y₂O₃. Fig 4(a) is the surface model of TiC (110), which is of nonpolar surfaces. Y₂O₃ (111) surface models exist three kinds of terminations, and all of them are of polarity surfaces. Fig 4(b)~(d) are Y-terminated, O-terminated(O over Y) and O-terminated(O over O) surface models of Y₂O₃ (111).

3.3.1 Surface energy of TiC

The convergence of the surface energy with the increase of atomic layer N is one of the means to prove the surface model achieved bulk like properties. The surface energy of TiC (110) model can be calculated by the Botteger Eqs. [30]:

$$\sigma_{\text{TiC}(110)} = \frac{1}{2A} (E_{\text{slab}}^N - N\Delta E) \quad (2)$$

$$\Delta E = (E_{\text{slab}}^N - E_{\text{slab}}^{N-2}) / 2 \quad (3)$$

where $\sigma_{\text{TiC}(110)}$ is the surface energy of TiC(110) model; E_{slab}^N and E_{slab}^{N-2} are the total energy of surface models with N and N-2 atomic layers, respectively; A is the surface area of the surface model.

The surface energies of TiC(110) model with different atomic layer number are listed in Table 2. When the layer number of the surface model reaches 11, TiC (110) surface energy is converged to 3.58 J/m² commendably. It indicates that 11-layered TiC (110) model can achieve convergence.

Table 2 Calculated surface energies of TiC(110) models

Layer (N)	5	7	9	11	13	15
Surface energy (J/m ²)	3.82	3.63	3.66	3.58	3.58	3.57

3.3.2 Surface energy of Y₂O₃

Surface energy of Y₂O₃(111) model can be calculated by equation as follow:

$$\sigma_{Y_2O_3(111)} = \frac{1}{2A} [E_{slab} - N_Y \mu_Y - N_O \mu_O] \quad (4)$$

where $\sigma_{Y_2O_3(111)}$ is the surface energy of Y₂O₃(111) model; A is the surface area of the model; E_{slab} is the total energy of surface model; N_Y and N_O are the numbers of Y atom and O atom in surface model respectively; μ_Y and μ_O are the chemical potentials of Y atom and O atom respectively.

The Y₂O₃ bulk unit energy $\mu_{Y_2O_3}^{bulk}$ can be calculated by equation as follow:

$$2\mu_Y + 3\mu_O = \mu_{Y_2O_3}^{bulk} \quad (5)$$

Combining equation (4) with equation (5), the equation of $\sigma_{Y_2O_3(111)}$ with only one variable (μ_O) is as follow:

$$\sigma_{Y_2O_3(111)} = \frac{1}{2A} [E_{slab} - \frac{N_Y}{2} \mu_{Y_2O_3}^{bulk} - (N_O - \frac{3}{2} N_Y) \mu_O] \quad (6)$$

In order to simplify the calculation, μ_O is regarded as μ_O^{bulk} approximatively. μ_O^{bulk} is the chemical potential of O atoms in Y₂O₃ bulk, and put its value into equation (6) to get $\sigma_{Y_2O_3(111)}$ values. The surface energy of 4~19 slabs Y-terminated Y₂O₃ (111) model is listed in Table 3. When the layer number of the model is more than 13, the surface energy can converge to 5.82 J/m², which indicates the interior of the model reach bulk like properties. The surface energy of 3~15 slabs O-terminated Y₂O₃ (111) model is listed in Table 4. When the layer number of the model is more than 12, the surface energy can converge to 1.27 J/m², which indicates the model attains a stable state.

Table 3 Calculated surface energies of Y₂O₃(111) Y-terminated models.

Layer(N)	4	7	10	13	16	19
Surface energy(J/m ²)	8.87	7.18	5.63	5.82	5.81	5.83

Table 4 Calculated surface energies of Y₂O₃(111) O-terminated models.

Layer(N)	3	6	9	12	15
Surface energy(J/m ²)	0.61	1.14	1.30	1.27	1.28

By the above calculations, 11-layered TiC(110) slab, 13-layered Y-terminated Y₂O₃(111) slab and 12-layered O-terminated (O over Y) Y₂O₃(111) slab are chosen to build interfaces. While O-terminated (O over O) Y₂O₃(111) slab cannot reach convergence due to its oxygen-rich surface, so it is not taken into account in the subsequent calculations.

3.4 Interfacial properties

Based on the lattice misfit calculation and surface convergence tests, four types of interface models were built with the consideration of different stacking modes. In ‘OT’ interface models, the first layer atoms of TiC slab are on the top-site of Y₂O₃ slab. In ‘HCP’ interface models, the first layer atoms of TiC slab are on the bridge-site of Y₂O₃ slab, and the second layer atoms of TiC slab are on the top-site of Y₂O₃ slab. For the convenience of expression, the interface models’ names can be simplified as follows: Y₂O₃/TiC Y-terminated OT interface is named as Y-TiC1; Y₂O₃/TiC Y-terminated HCP interface named as Y-YiC2; Y₂O₃/TiC O-terminated OT interface named as O-TiC1 and Y₂O₃/TiC O-terminated HCP interface named as O-YiC2. The interface models are shown in Fig 5(a) ~ (d), and Fig 5(e) ~ (h) are the bottom views of the interface models accordingly.

3.4.1 Interfacial electronic structures and bonding characters

The combination of the interfacial atoms is related to the interface electronic structure and bonding character, which can be represented by electron density and charge density difference. Electron density can be obtained directly from the calculation and charge density difference K_d can be obtained by Eqs. [31]:

$$K_d = K_{total} - K_{TiC(110)} - K_{Y_2O_3(111)} \quad (7)$$

where K_{total} is the total charge density of the interface system; $K_{TiC(110)}$ and $K_{Y_2O_3(111)}$ are the charge density of isolated TiC slab and Y_2O_3 slab in the same super cell respectively.

Fig 6 is the charge density of Y_2O_3/TiC Y-terminated interface. Fig 6 (a) and Fig 6 (b) are the charge density of Y-TiC1 interface section 1 and section 2 respectively. It can be seen obviously, that the bonding between O atom and Ti atom is strong, while the bonding between C atom and Y atom as well as Ti atom and Y atom is relatively weak, and the bonding between O atom and C atom is not obvious. Fig 6 (c) and Fig 6 (d) are the charge density of Y-TiC2 interface section 1 and section 2 respectively. The bonding situation of Y-TiC2 interface is similar to that of Y-TiC1.

Fig 7 is the charge density of Y_2O_3/TiC O-terminated interface. Fig 7 (a) and Fig 7 (b) are the charge density of O-TiC1 interface section 1 and section 2 respectively. It can be seen obviously, that the bonding between O atom and C atom as well as O atom and Ti atom is very strong, while the distance of Y atom and C atom as well as Y atom and Ti atom is too far to form chemical bond. Fig 7 (c) and Fig 7 (d) are the charge density of O-TiC2 interface section 1 and section 2 respectively. It can be seen obviously, that the bonding between O atom and C atom as well as O atom and Ti

atom is very strong, while the bonding between Y atom and Ti atom as well as Y atom and C atom is fairly weak.

Fig 8 is the charge density difference of Y_2O_3/TiC Y-terminated interface. Fig 8 (a) and Fig 8 (b) are the charge density difference of Y-TiC1 interface after fully relaxation. In Fig 8 (a), a charge accumulation region is appeared between C atom and Y atom, which indicates the existence of charge sharing. In Fig 8 (b), a large charge depletion region is appeared round Ti atom, while a large charge accumulation region is appeared round the adjacent O atom, which implies the bonding between Ti atom and O atom has a strong polarity. Fig 8 (c) and Fig 8 (d) are the charge density differences of Y-TiC2 interface after fully relaxation. From the strong charge accumulation round O atom and a charge depletion region round Ti atom in Fig 8 (c), the bonding between O atom and Ti atom is a polar covalent bond. From the charge accumulation region between Y atom and C atom in Fig 8 (d), the bonding between Y atom and C atom is a covalent bond. A charge depletion region appeared in the direction of the O-C bonding nearby the C atom, which indicates the polar covalent bond can form between O atom and C atom.

Table 5 Mulliken population analysis of Y-TiC interfaces.

Bond	O ₁ -Ti ₂	C ₂ -Y ₂	Ti ₁ -Y ₁	C ₂ -O ₂
Y-TiC1	0.27	0.48	0.10	
Y-TiC2	0.16	0.38		-0.05

Table 5 lists the mulliken population of the Y-TiC interface system. The population of O₁-Ti₂ bond and C₂-Y₂ bond in Y-TiC1 interface is 0.27 and 0.48, which indicate that polar covalent bonds are formed between O atom and Ti atom as well as C atom and Y atom. The population of Ti₁-Y₁ bond is 0.10, so it is of some

metallic character. The population of Y-TiC2 interface is 0.16 for O-Ti bond and 0.38 for C-Y bond. Together with the charge differences, the bonding of Y-TiC1 and Y-TiC2 interfaces is a mixture of polar covalent bonds and metallic ones.

Fig 9 is the charge density difference of Y₂O₃/TiC O-terminated interface. Fig 9(a) and Fig 9(b) are the charge density differences of O-TiC1 interface after fully relaxation. The charge depletion regions are appeared around C atom and Ti atom, and the charge accumulation regions are appeared around C atom and O atom. The interatomic charge accumulation region is deflected to O atom, which indicates the bond between them has a strong polarity. Fig 9(c) and Fig 9(d) are the charge density differences of O-TiC2 interfaces after fully relaxation. The charge accumulation region is appeared around O atom and the charge depletion region is appeared around Ti atom. The charge accumulation regions and charge sharing phenomenon are appeared between C atom and O atom as well as Y atom and C atom, which indicate their bondings are covalent bonds.

Table 6 Mulliken population analysis of O-TiC interfaces.

Bond	Ti ₁ -O ₁	Ti ₁ -O ₂	C ₁ -O ₁	C ₂ -Y ₂	Ti ₂ -O ₂	Ti ₂ -O ₃	C ₂ -O ₂
O-TiC1	0.54		-0.04		-0.05		0.76
O-TiC2	-0.19	0.40	0.85	0.37	0.20	0.29	

Table 6 lists the mulliken population of the O-TiC interface system. The population of C₂-O₂ bond in O-TiC1 interface is 0.76. The population of Ti₁-O₁ bond in O-TiC1 interface is 0.54. Together with the charge differences, the bonding between O atom and Ti atom as well as C atom and O atom is polar covalent bond. The population of C₁-O₁ bond in O-TiC2 interface is 0.85, which indicates the bonding between C atom and O atom is covalent bond. The populations of the three

Ti-O bonds are 0.40, 0.20 and 0.29 respectively. The charge accumulated regions are appeared around O atom and the charge depletion regions are appeared around Ti atom, which indicates the polar covalent bonds are formed between them. The population of Y₂-C₂ bond is 0.37 and the charge accumulation region deflects to C atom, which indicates the polar covalent bond forms between them.

Fig 10 is the DOS of Y₂O₃/TiC interface. The DOS of the four interfaces all have peaks at Fermi level, which indicates the metallic properties of the interfaces. It is obvious that the peaks at Fermi level are mainly composed of d orbital and p orbital, while the contribution of s orbital is very small. From Fig 10(a), the DOS peak of Y-TiC1 interface is the most sharp and its pseudogap is the widest, which indicate the strong covalent bonding interaction in the interface. From Fig 10(b), the DOS peak of Y-TiC2 interface is also very sharp, and the width of pseudogap is close to that of Y-TiC1. From Fig 10(c) and Fig 10(d), the pseudogaps of O-TiC1 interface and O-TiC2 interface are significantly lower than those of Y-TiC1 interface and Y-TiC2 interface, so their covalency is weaker relatively. Different from Y-TiC1 and Y-TiC2 interface, the p orbital's contribution to the peak intensity near Fermi level is greater than d orbital in O-TiC1 and O-TiC2 interfaces obviously, which indicates that ionic bond and polar covalent bond are formed in the two interfaces.

3.4.2 Interface stability

The interface adhesive work and interfacial energy are closely related to the interfacial electronic structures and bond characters, which can be used to evaluate the stability of interface system.

Interface adhesive work can be defined as the reversible work required in separating an interface into two free surfaces, which can be a reflex of the bonding strength of the interface structure [32]. The interface adhesive work W_{ad} can be calculated by Eqs. [33]:

$$W_{ad} = \frac{1}{A} (E_{TiC} + E_{Y_2O_3} - E_{TiCY_2O_3}) \quad (8)$$

where $E_{TiCY_2O_3}$ is the total energy of the interface structure; E_{TiC} and $E_{Y_2O_3}$ are the total energies of isolated TiC(110) and Y₂O₃(111) surface models; A is the interface area.

Table 7 lists W_{ad} and interfacial spacing d_0 . According to W_{ad} , the stability of the interface models is ranked as follows: Y-TiC1 < Y-TiC2 < O-TiC1 < O-TiC2. Among them, the O-TiC2 interface has the largest W_{ad} (6.07 J/m²) and the smallest d_0 (0.85 Å), which indicates that its adhesive strength is the strongest among all of the interfaces.

Table 7 Calculated adhesion work W_{ad} and interfacial separation d_0 of the Y-TiC and O-TiC interfaces.

Mold	W_{ad} (J/m ²)	d_0 (Å)
Y-TiC1	0.35	1.79
Y-TiC2	0.37	1.77
O-TiC1	4.78	1.31
O-TiC2	6.07	0.85

The interfacial energy is also an important parameter to evaluate the interface stability. Generally, the smaller the interfacial energy is, the interface structure is more stable [16]. The interfacial energy γ can be calculated by Eqs. [34]:

$$\gamma = \sigma_{TiC} + \sigma_{Y_2O_3} - W_{ad} \quad (9)$$

where σ_{TiC} and $\sigma_{Y_2O_3}$ are the surface energy of TiC(110) and Y₂O₃(111) models; W_{ad} is the adhesive work of Y₂O₃/TiC interface.

Table 8 Interface energies of the $Y_2O_3(111)/TiC(110)$ interfaces.

Mold	Y-TiC1	Y-TiC2	O-TiC1	O-TiC2
γ (J/m ²)	9.05	9.03	0.07	-1.22

Table 8 lists γ of the $Y_2O_3(111)/TiC(110)$ interface models. According to the interfacial energy γ , the stability of the interface models is ranked as follows: O-TiC2 > O-TiC1 > Y-TiC2 > Y-TiC1. Among them, the O-TiC2 interface has the smallest γ (-1.22J/m²), which indicates that O-TiC2 interface is the most stable. Furthermore, γ of O-TiC2 interface is lower than zero, which indicates its good thermodynamic stability. The solid-solid interfacial energy is higher than zero [13]. From the above analysis, Y_2O_3 can act as the heterogeneous nucleus of TiC.

3.5 Experimental research on the interface relations of Y_2O_3/TiC

3.5.1 Elemental distribution analysis

Fig 11 shows the microstructure of the hypereutectic Fe-Cr-C-Ti- Y_2O_3 coating and the elemental distribution mappings of elements Cr, Ti and Y. From Fig 11(a), the microstructure of the hypereutectic Fe-Cr-C-Ti- Y_2O_3 coating includes gray primary M_7C_3 carbides, black flower-like TiC particles and base metal. From Fig 11(b), the green polygonal region is rich in Cr, which is the primary M_7C_3 carbide. The element analysis of its central nearby flower-like area is as shown in Fig 11(c), and element Ti enriched purple area is the TiC particle precipitated before primary M_7C_3 carbide. Element Y analysis of TiC particles in Fig 11(c) is as shown in Fig 11(d). The enrichment of element Y can be found in the center of Ti enriched area, which indicates that the Y_2O_3 exists in the center of TiC particles.

3.5.2 TEM observation of the heterogeneous nucleation interface

Fig 12 shows the TEM images of the hypereutectic Fe-Cr-C-Ti- Y_2O_3 coating.

Fig 12(a) is the bright field image of the flower-like particle in primary M_7C_3 carbide. Selected area diffraction patterns (SADPs) of its "pistil" and "petal" are executed respectively, and the corresponding dark field images are shown in Fig 12(b) and Fig 12(c). According to the SADPs in the upper right corner of Fig 12(b) and Fig 12(c), the interior "pistil" is Y_2O_3 and the exterior "petal" is TiC. TiC grows dependently on Y_2O_3 and they are tightly combined. The previous calculation results indicate that Y_2O_3 can be the heterogeneous nucleus of TiC from a theoretical point and the experimental results furtherly verify the calculation results.

3.6 Discussion

From the above analysis, we can find that the charge sharing phenomenon of O-TiC1 and O-TiC2 interfaces is stronger than that of Y-TiC1 and Y-TiC2 interfaces and the covalent bonding between O-TiC2 interface is the strongest, which accord with the analysis of interface adhesive work and the interfacial energy. Based on the thermodynamic analysis and the electronic analysis, the O-TiC2 interface is the most stable one of all the interface models. S.X. Jin et al. [16] investigated the interface structure, energy and electronic properties of TaN/ReB₂ multilayers based on DFT. They found that Re-N2 interface is the most stable interface with the highest W_{ad} (0.969 eV/Å²) and the lowest interfacial energy (-1.327 eV/Å²). In this work, O-TiC2 interface is the most stable interface with the highest W_{ad} (6.07 J/m²) and the lowest interfacial energy (-1.22 J/m²). And the negative value of the interfacial energy of the O-TiC2 interface reveals its supernormal stability, because of the solid-solid interfacial energy is higher than zero. The TEM images indicate that TiC is

crystallized beside Y_2O_3 particle and they are tightly combined, which proves that Y_2O_3 can act as the heterogeneous nucleus of TiC. Therefore, Y_2O_3 can refine TiC and increase the number of TiC particles in hypereutectic Fe-Cr-C-Ti- Y_2O_3 coating. The number of the heterogeneous nucleus of primary M_7C_3 carbide is increased and its size can be refined further. S. Buytoz, A. Orhan, A.K. Gur and U. Caligulu [35] found that the primary M_7C_3 carbides are non-uniformly distributed in γ -Fe, Ni eutectic matrix. On this basis, we also hope to homogenize the non-uniformly distribution of the primary M_7C_3 carbides to improve the mechanical properties of Fe-Cr-C coatings.

4. Conclusions

1). The Bramfitt two-dimensional lattice misfit of $Y_2O_3(111)/TiC(110)$ is 8.6%, which indicates Y_2O_3 can be medium effective heterogeneous nucleus of TiC.

2). The bonding of TiC bulk is a mixture of covalent bond and metallic bond, while that of Y_2O_3 bulk is a mixture of ionic bond and metallic bond. Four interfaces are built based on the Bramfitt two-dimensional lattice misfit and stacking modes, whose interface bonding is a mixture of covalent, metallic and ionic bonds (or, as a combination of polar covalent bond and metallic bond).

3). The interface adhesive works are ranked as $W_{ad} (O-TiC2) > W_{ad} (O-TiC1) > W_{ad}(Y-TiC2) > W_{ad}(Y-TiC1)$ and the interfacial energies are ranked as $\gamma (O-TiC2) > \gamma (O-TiC1) > \gamma (Y-TiC2) > \gamma (Y-TiC1)$. According to W_{ad} and γ , the O-TiC2 interface is the most stable with the largest interface adhesive work (6.07 J/m²) and the smallest interfacial energy (-1.22 J/m²). The calculation results

indicate that Y_2O_3 can be the heterogeneous nucleus of TiC theoretically.

4). The experimental results show that Y_2O_3 exists inside TiC particle and they are tightly combined, which proves the heterogeneous nucleus role of Y_2O_3 on TiC. In this way, Y_2O_3 can refine TiC and increase the number of it. The primary M_7C_3 carbides can be refined further.

Acknowledgement

The authors would like to express their gratitude for projects supported by the National Natural Science Foundation of China (No. 51471148 and No.51771167), the Hebei province Basic Research Foundation of China (No. 16961008D).

References :

- [1] S. Buytoz, Microstructural properties of M_7C_3 eutectic carbides in a Fe-Cr-C alloy, *Mater. Lett.* 60 (2006) 605-608.
- [2] T. Yildiz, A. K. Gür, Microstructural characteristic of N_2 shielding gas in coating FeCrC composite to the surface of AISI 1030 steel with PTA method, *Arch. Metall. Mater.* 56 (3) (2011) 723-729.
- [3] A. K. Gür, S. Kaya, Abrasive wear resistance optimization of three different carbide coatings by the Taguchi method, *Mater. Test.* 59 (5) (2017) 450-455.
- [4] A. K. Gür, C. Ozay, A. Orhan, S. Buytoz, U. Caligulu, N. Yigitturk, Wear properties of Fe-Cr-C and B_4C powder coating on AISI 316 stainless steel analyzed by the Taguchi method, *Mater. Test.* 56 (5) (2014) 393-398.
- [5] A. K. Gür, Investigating wear behavior by using Taguchi method FeCrC/ B_4C powder alloys coating by plasma transferred arc weld surfacing, *Mater. Test.* 55 (6) (2013) 462-467.
- [6] L.I. Joansson, Electronic and structural properties of transition-metal carbide and nitride surfaces, *Surf. Sci. Rep.* 21 (1995) 177-250.
- [7] T. Sun, X.Z. Wu, R. Wang, W.G. Li, Q. Liu, First-principles study on the adhesive properties of Al/TiC interfaces: Revisited, *Comput. Mater. Sci.* 126 (2017) 108-120.
- [8] M. Fattahi, M. Mohammady, N. Sajjadi, M. Honarmand, Y. Fattahi, S. Akhavan, Effect of TiC nanoparticles on the microstructure and mechanical properties of gas tungsten arc welded aluminum joints, *J. Mater. Process. Technol.* 217 (2015)

21-29.

- [9] K.K. Patel, V. kumar, R. Purohit, G.K.Gupta, O.P. Modi, Effect of Ultrasonic Stirring on Changes in Microstructure and Mechanical Properties of Cast In-situ Al 5083 alloy Composites Containing 5wt.% and 10wt.% TiC particles, Mater. Today. Proc. 4 (2017) 3494-3500.
- [10] K. Hamano, S. Ohta, Y. Ozaki, Effects of rare earth oxides on sintering of alumina, J. Ceram. Assoc. Jpn. 87 (1979) 632–641.
- [11] A. Noviyanto, D.H. Yoon, Rare-earth oxide additives for the sintering of silicon carbide, Diam. Relat. Mater. 38 (6) (2013) 124-130.
- [12] Y. Chen, Y.C. Wu, F.W. Yu, J.L. Chen, Microstructure and mechanical properties of tungsten composites co-strengthened by dispersed TiC and La₂O₃ particles, Int. J. Refract. Met. Hard Mater. 26 (2008) 525-529.
- [13] S. Liu, Y.F. Zhou, X.L. Xing, J.B. Wang, Q.X. Yang, Refining effect of TiC on primary M₇C₃ in hypereutectic Fe-Cr-C harden-surface welding coating: Experimental research and first-principles calculation, J. Alloys. Compd. 691 (2017) 239-249.
- [14] X. Yun, Y.F. Zhou, J. Yang, X.L. Xing, X.J. Ren, Y.L. Yang, Q.X. Yang, Refinement of nano-Y₂O₃ on microstructure of hypereutectic Fe-Cr-C hardfacing coatings, J. Rare. Earth. 33 (2015) 671-678.
- [15] S.Q. Wang, H.Q. Ye, Theoretical studies of solid-solid interfaces, Curr. Opin. Solid State Mater. Sci. 10 (2006) 26-32.
- [16] S.X. Jin, N. Liu, S. Zhang, D. Li, The simulation of interface structure, energy

and electronic properties of TaN/ReB₂ multilayers using first-principles, Surf. Coat. Tech. In Press.

- [17] K. Li, Z.G. Sun, F. Wang, N.G. Zhou, X.W. Hu, First-principles calculations on Mg/Al₄C₃ interfaces, Appl. Surf. Sci. 270 (2013) 584-589.
- [18] J. Li, M. Zhang, Y. Zhou, G.X. Chen, First-principles study of Al/Al₃Ti heterogeneous nucleation interface, Appl. Surf. Sci. 307 (2014) 593-600.
- [19] G. Kresse, J. Harner, Ab initio molecular dynamics for liquid metals, Phys. Rev. B. 47 (1993) 558-561.
- [20] D.R. Hamann, M. Schluter, C. Chiang, Norm-Conserving Pseudopotentials, Phys. Rev. Lett. 43 (1979) 1494-1497
- [21] N. Troullier, J.L. Martins, Efficient pseudopotentials for plane-wave calculations Phys. Rev. B. 43 (1991) 1993-2006.
- [22] H.J. Monkhorst, J.D. Pack, Special points for Brillouin-zone integrations, Phys. Rev. B. 13 (1976) 5188-5192.
- [23] T.H. Fischer, J. Almlof, General methods for geometry and wave function optimization, J. Phys. Chem. 96 (1992) 9768-9774.
- [24] B.G. Pfrommer, M. Côté, S.G. Louie, M.L. Cohen, Relaxation of crystals with the quasi-Newton method, J. Comput. Phys. 131 (1997) 133-140.
- [25] B.L. Bramfitt, The Effect of Carbide and Nitride Additions on the Heterogeneous Nucleation Behavior of Liquid Iron, Metall. Trans. 1 (7) (1970) 1987-1995.
- [26] S. Katagiri, N. Ishizawa, A new high temperature modification of face-centered cubic Y₂O₃, Powder Diffr. 8 (1) (1993) 60-60.

- [27] V.P. Zhukov, V.A. Gubanov, O. Jepsen, N.E. Christensen, O.K. Andersen, Calculated energy-band structures and chemical bonding in titanium and vanadium carbides, nitrides and oxides, *J. Phys. Chem. Solids.* 49 (7) (1988) 841-849.
- [28] D.J. Wilson, B. Winkler, E.A. Juarez-Arellano, A. Friedrich, K. Knorr, C.J. Pickard, V. Milman, Virtual crystal approximation study of nitridosilicates and oxonitridoaluminosilicates, *J. Phys. Chem. Solids.* 69 (7) (2008) 1861-1868.
- [29] X.Z. Wu, T. Sun, R. Wang, L.L. Liu, Q. Liu, Energy investigations on the adhesive properties of Al/TiC interfaces: first-principles study, *Physica B* 449 (1) (2014) 269-273.
- [30] J. Boettger, Nonconvergence of surface energies obtained from thin-film calculations, *Phys. Rev. B.* 49 (23) (1994) 16798-16800.
- [31] V. Fiorentini, M. Methfessel, Extracting convergent surface energies from slab calculations, *J. Phys. Condens. Matter* 8 (36) (1996) 6525-6529.
- [32] J. Guo, L.G. Liu, S. Liu, Y.F. Zhou, X.W. Qi, X.J. Ren, Q.X. Yang, Stability of eutectic carbide in Fe-Cr-Mo-W-V-C alloy by first-principles calculation, *Mater. Des.* 106 (2016) 355-362.
- [33] Y.J. Xian, R.Z. Qiu, X. Wang, P.C. Zhang, Interfacial properties and electron structure of Al/B₄C interface: A first-principles study, *J. Nucl. Mater.* 478 (2016) 227-235.
- [34] A. Ernst, G. van der Laan, W.M. Temmerman, S.S. Dhesi, Z. Szotek, Contesting results for magnetic moments in nickel thin films, *Phys. Rev. B.* 62 (14) (2000)

9543-9547.

- [35] S. Buytoz, A. Orhan, A. Kaya Gür and U. Caligulu, Microstructural properties of Fe-Cr-C and B₄C powder alloy coating on stainless steel by plasma transferred arc weld surfacing, Arab. J. Sci. Eng. 38 (2013) 2197-2204.

Fig. 1 Crystal structures

(a) TiC (b) Y_2O_3

Fig. 2 Bulk property of TiC

(a) Calculated electronic phonon dispersion (b) bond structure (c) density of states

Fig. 3 Bulk property of Y_2O_3

(a) Calculated electronic phonon dispersion (b) bond structure (c) density of states

Fig. 4 Surface models of TiC and Y_2O_3

(a) TiC(110) (b) Y_2O_3 (111)Y-terminated

(c) Y_2O_3 (111)O-terminated(O over Y) (d) Y_2O_3 (111)O-terminated(O over O)

Fig. 5 Interface models

(a) Y-TiC1 (b) Y-TiC2 (c) O-TiC1 (d) O-TiC2

(e) ~ (h) top views of the interface models

Fig. 6 Charge density of Y_2O_3 /TiC interface

(a) Y-TiC1 interface section 1 and (b) section 2, (c) Y-TiC2 interface section 1 and (d) section 2

Fig. 7 Charge density of Y_2O_3 /TiC interface

(a) O-TiC1 interface section 1 and (b) section 2, (c) O-TiC2 interface section 1 and (d) section 2.

Fig. 8 Charge density difference of Y_2O_3 /TiC interface

(a) Y-TiC1 interface section 1 and (b) section 2, (c) Y-TiC2 interface section 1 and (d) section 2.

Fig. 9 Charge density difference of Y_2O_3 /TiC interface

(a) O-TiC1 interface section 1 and (b) section 2, (c) O-TiC2 interface section 1 and (d) section 2.

Fig. 10 Density of states of Y_2O_3 /TiC interface

(a) Y-TiC1 interface (b) Y-TiC2 interface (c) O-TiC1 interface (d) O-TiC2 interface

Fig. 11 Microstructure of Fe-Cr-C-Ti- Y_2O_3 coating and elemental distribution mappings of elements

(a) Microstructure (b) Cr (c) Ti (d) Y

Fig. 12 TEM images of Fe-Cr-C-Ti- Y_2O_3 coating

(a) bright field image of the flower-like particle (b) SADPs of "pistil" (c) SADPs of "petal"

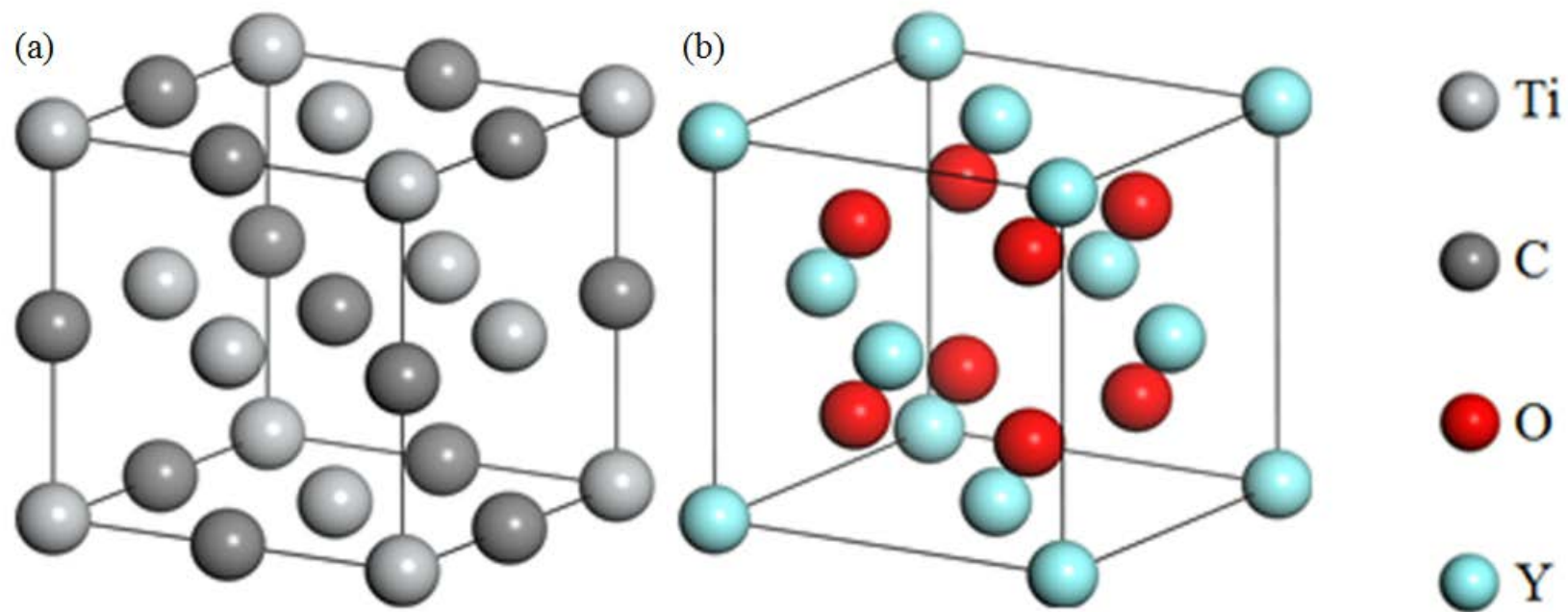


Fig.1

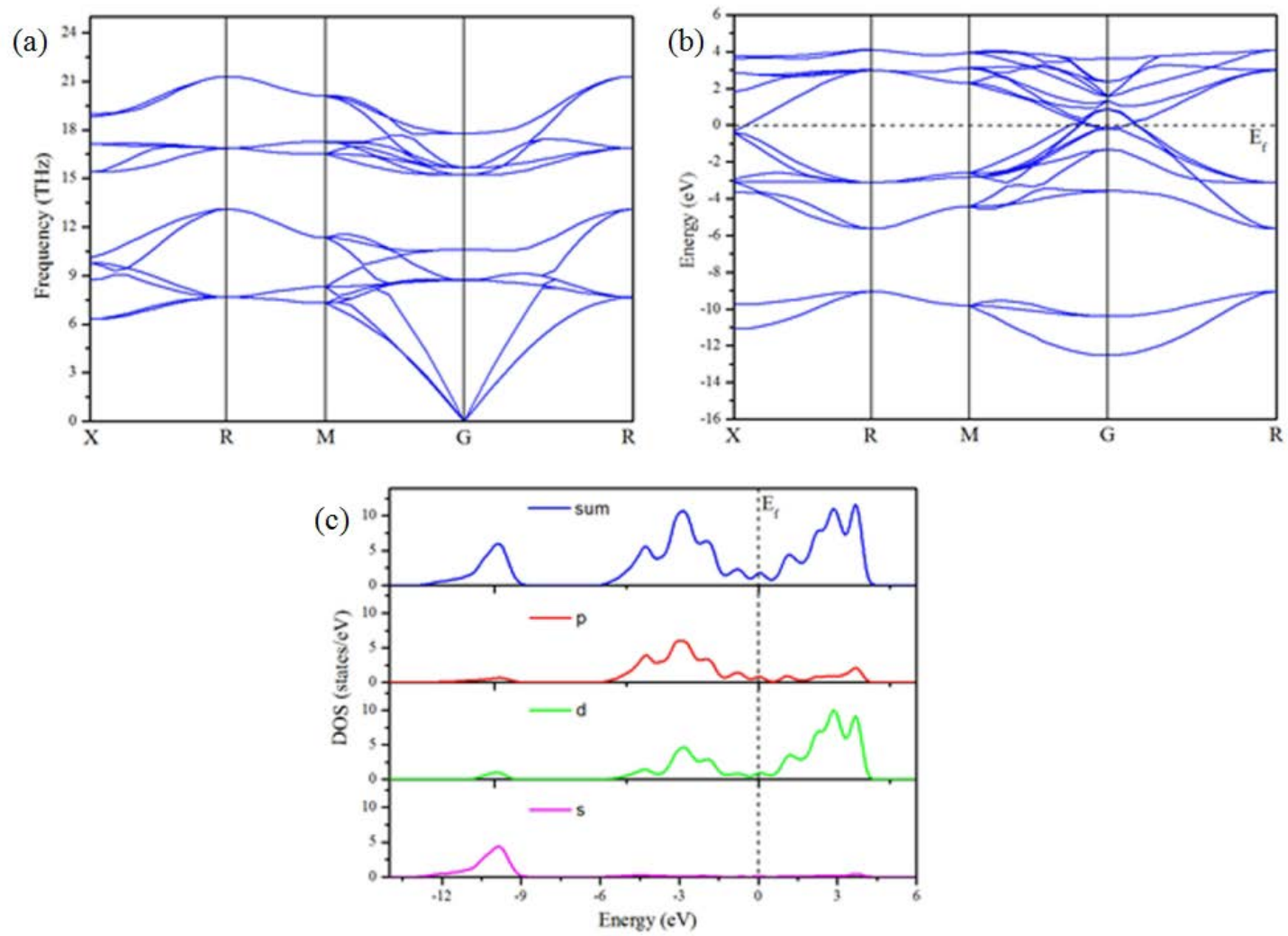


Fig. 2

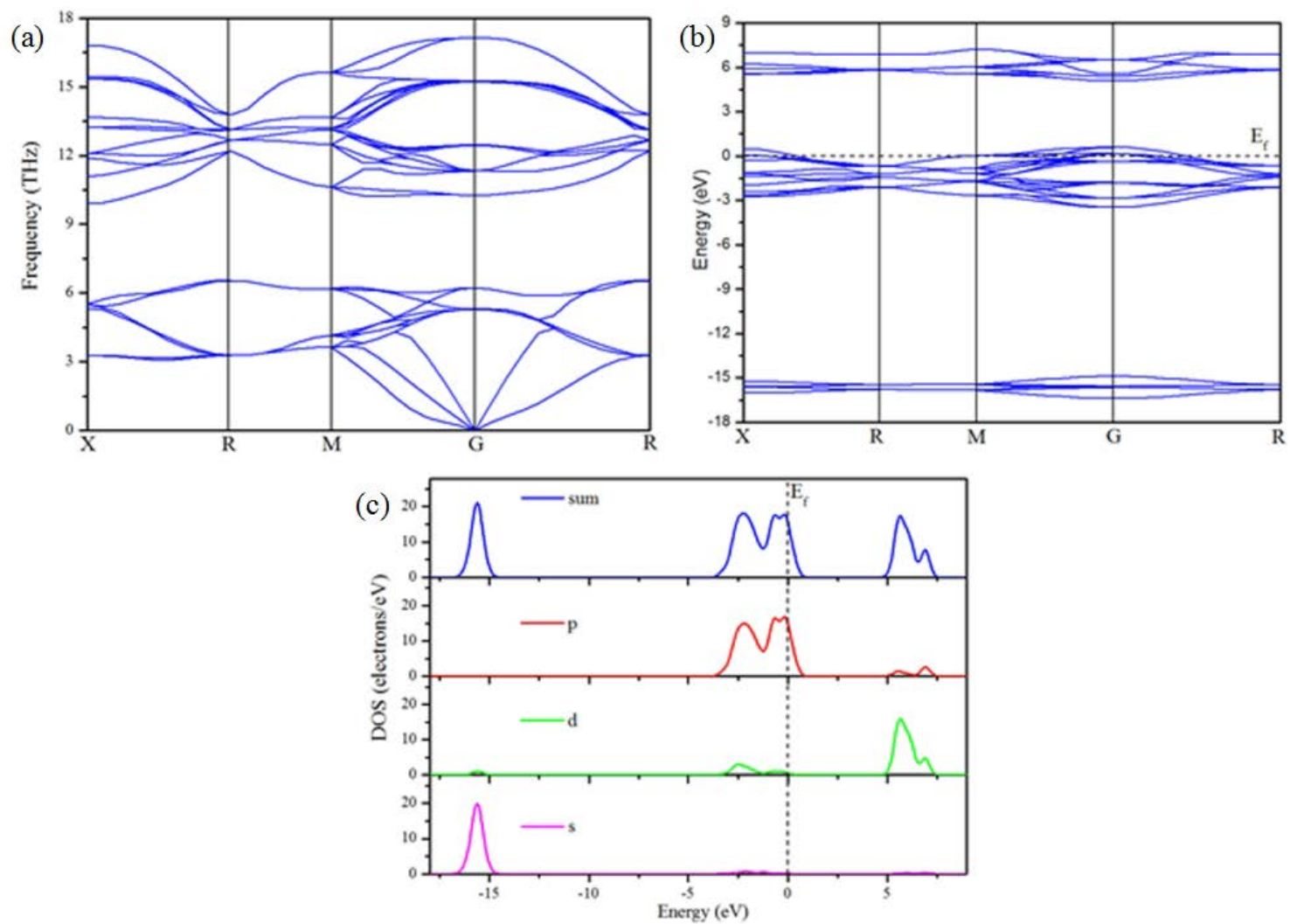
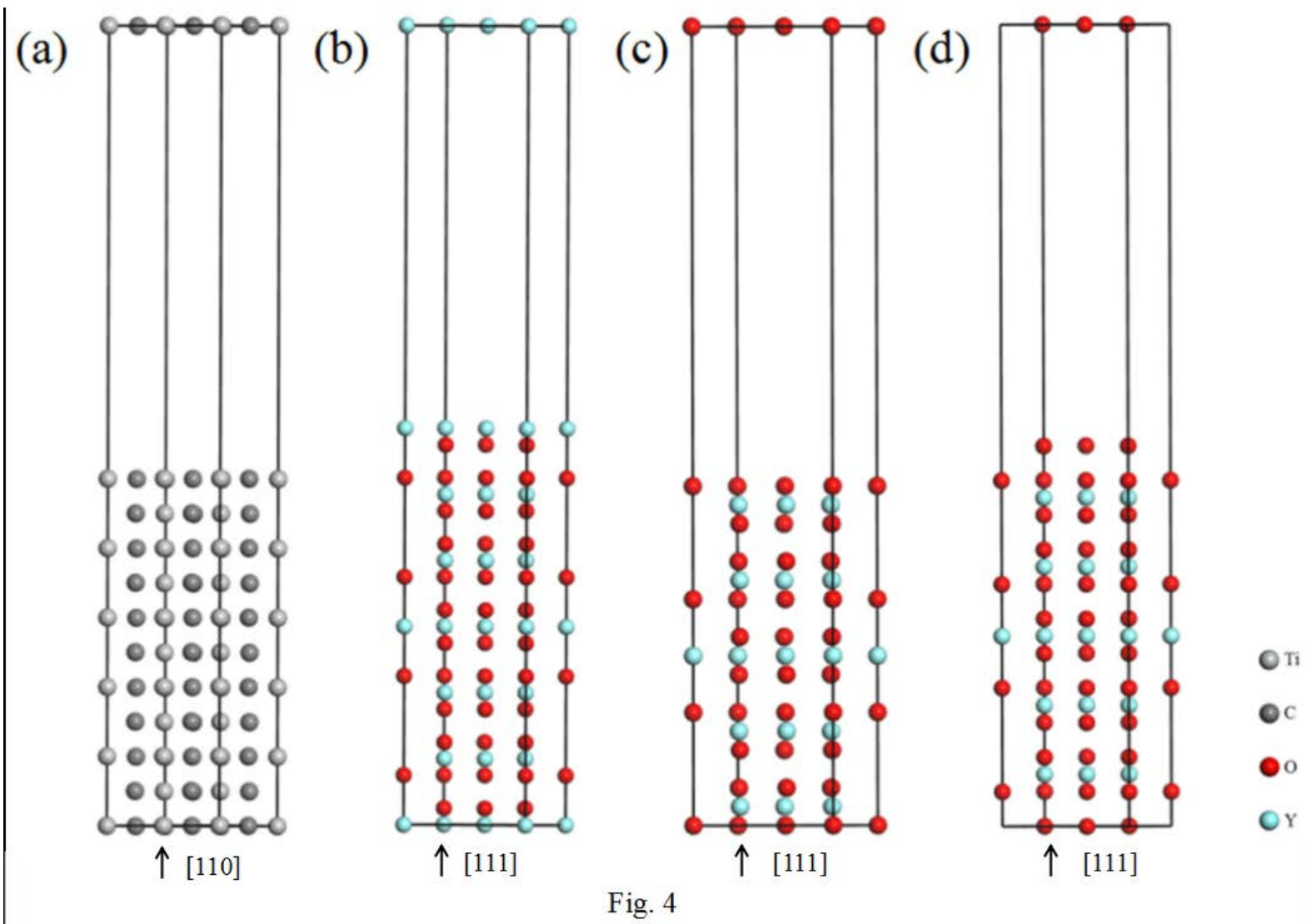


Fig. 3



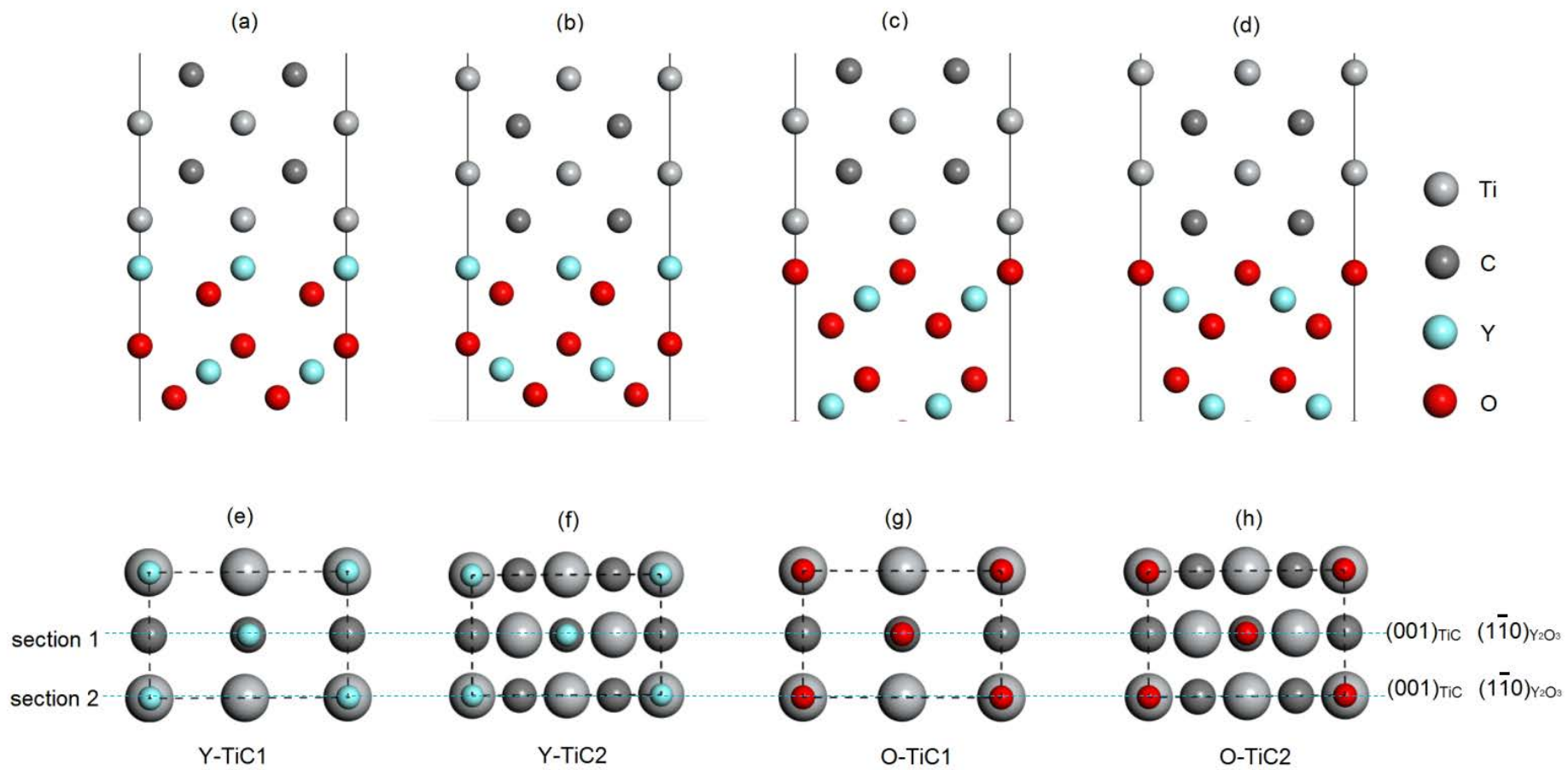


Fig.5

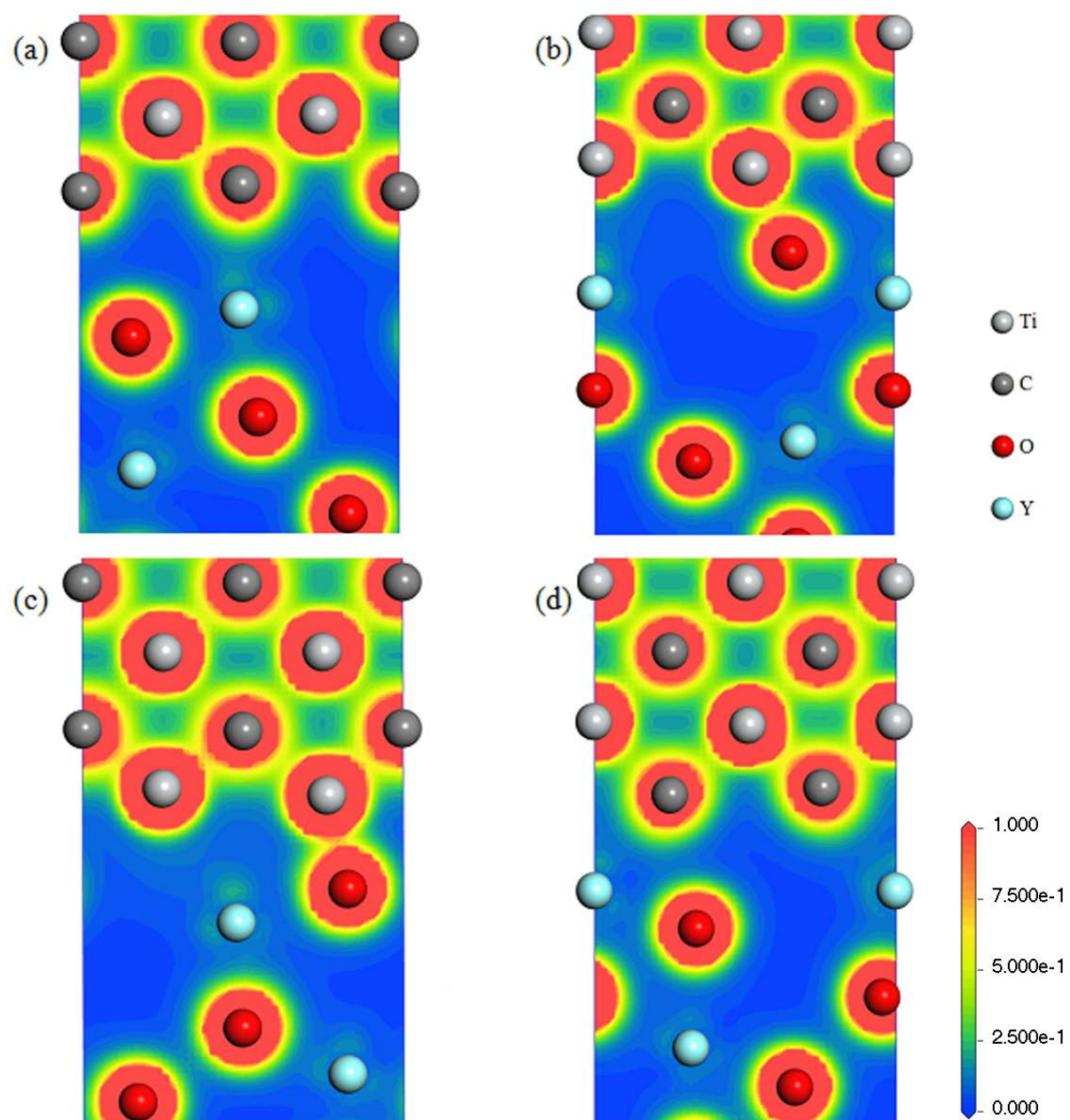


Fig. 6

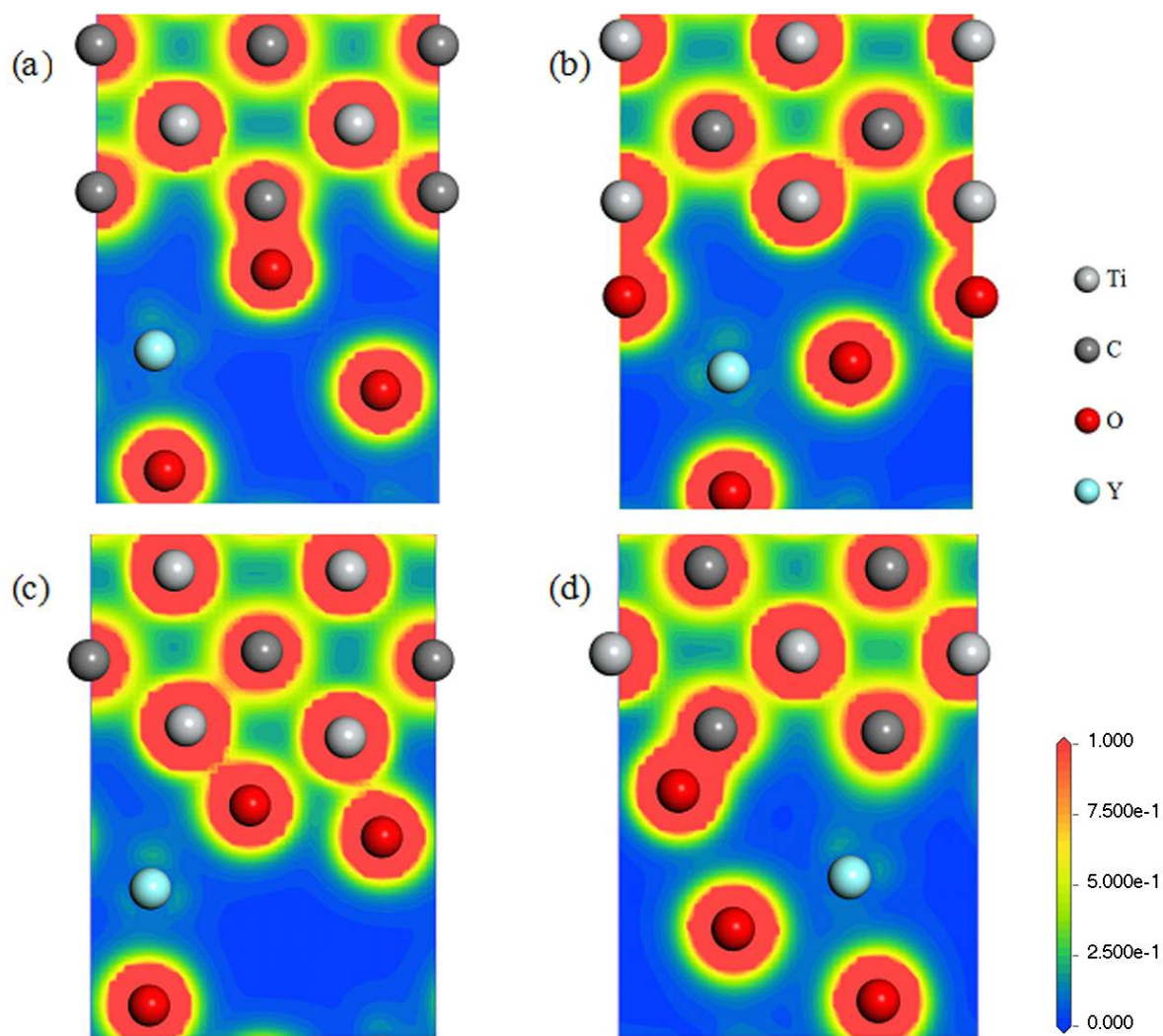


Fig. 7

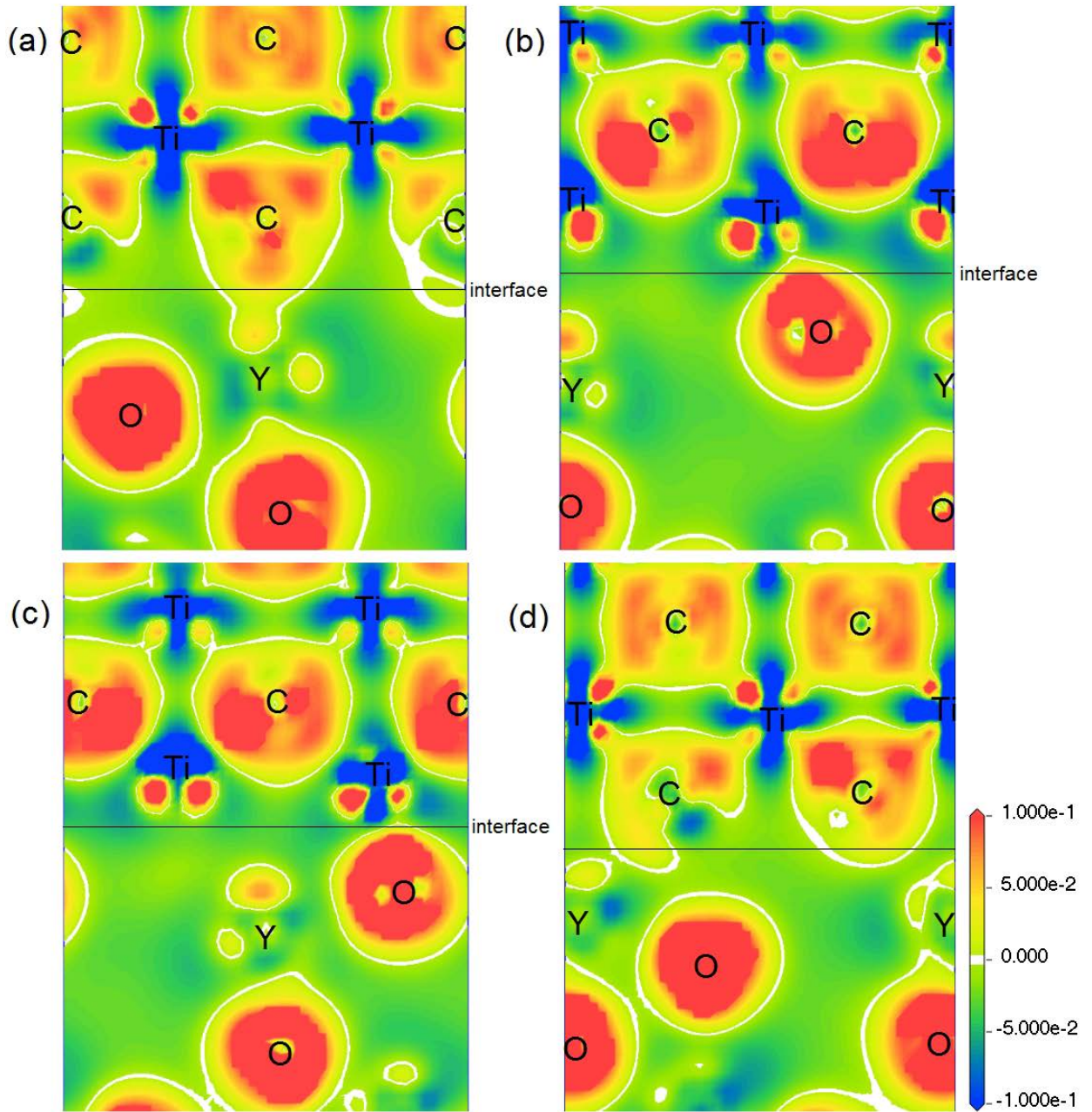


Fig.8

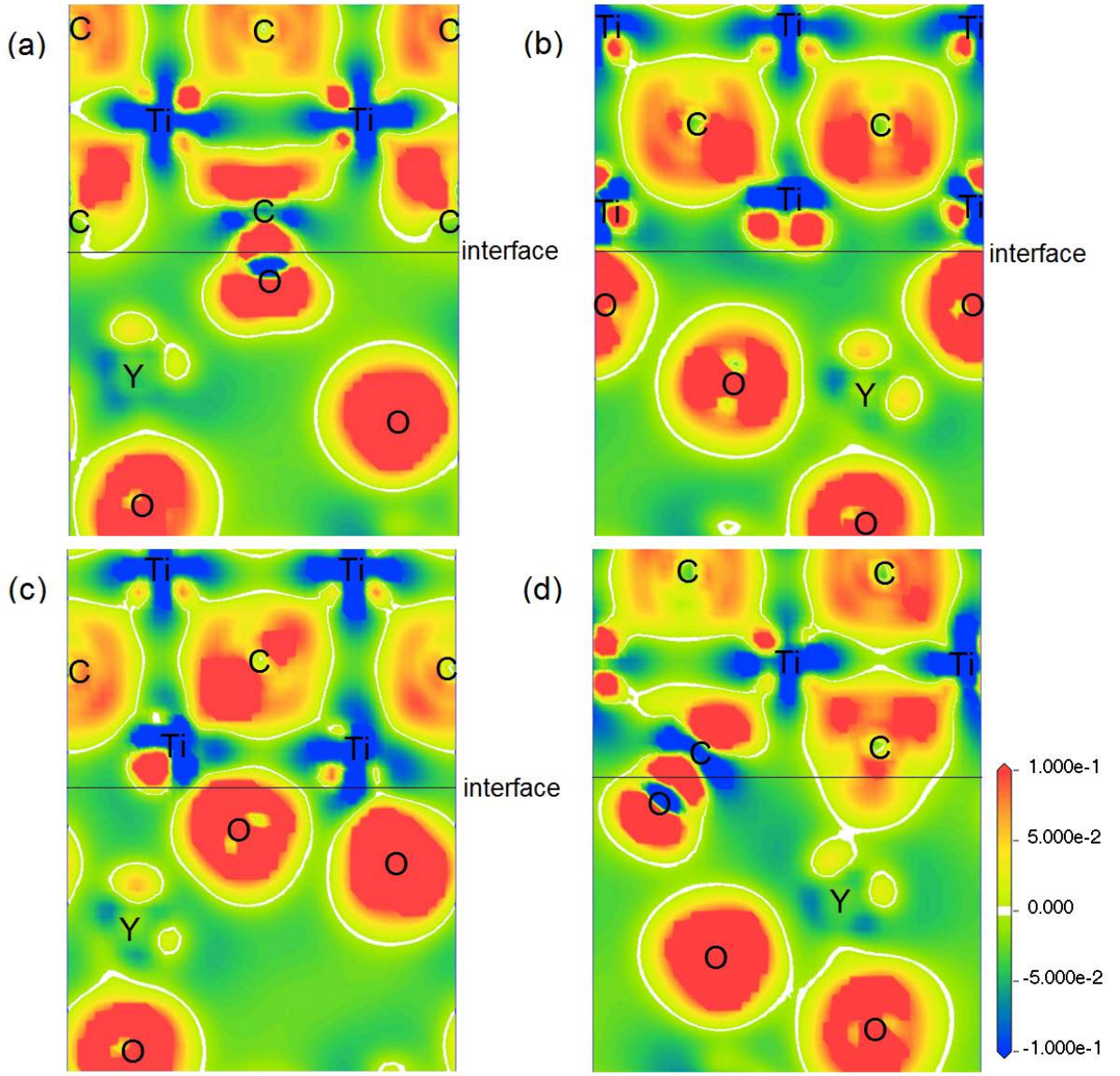


Fig.9

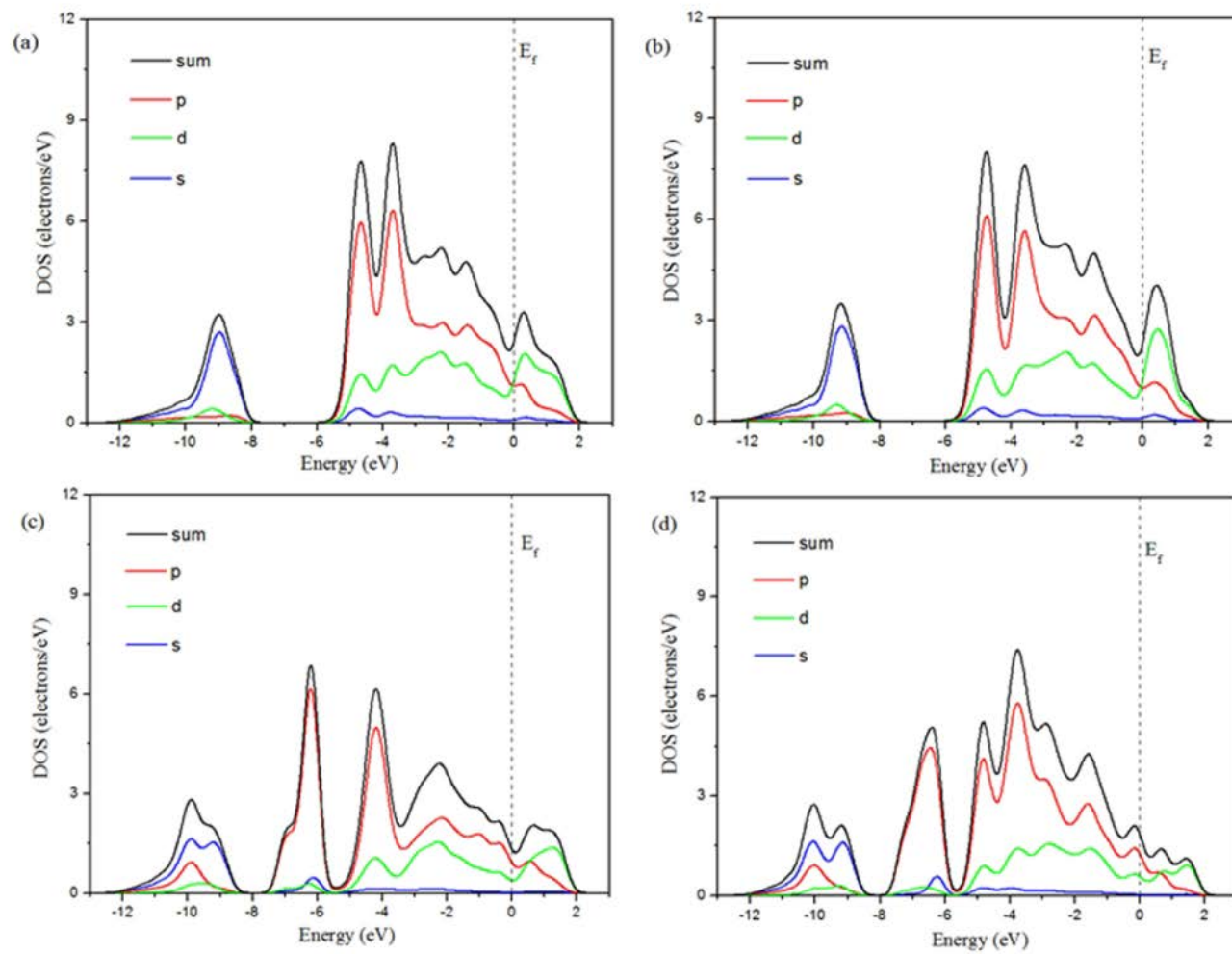


Fig. 10

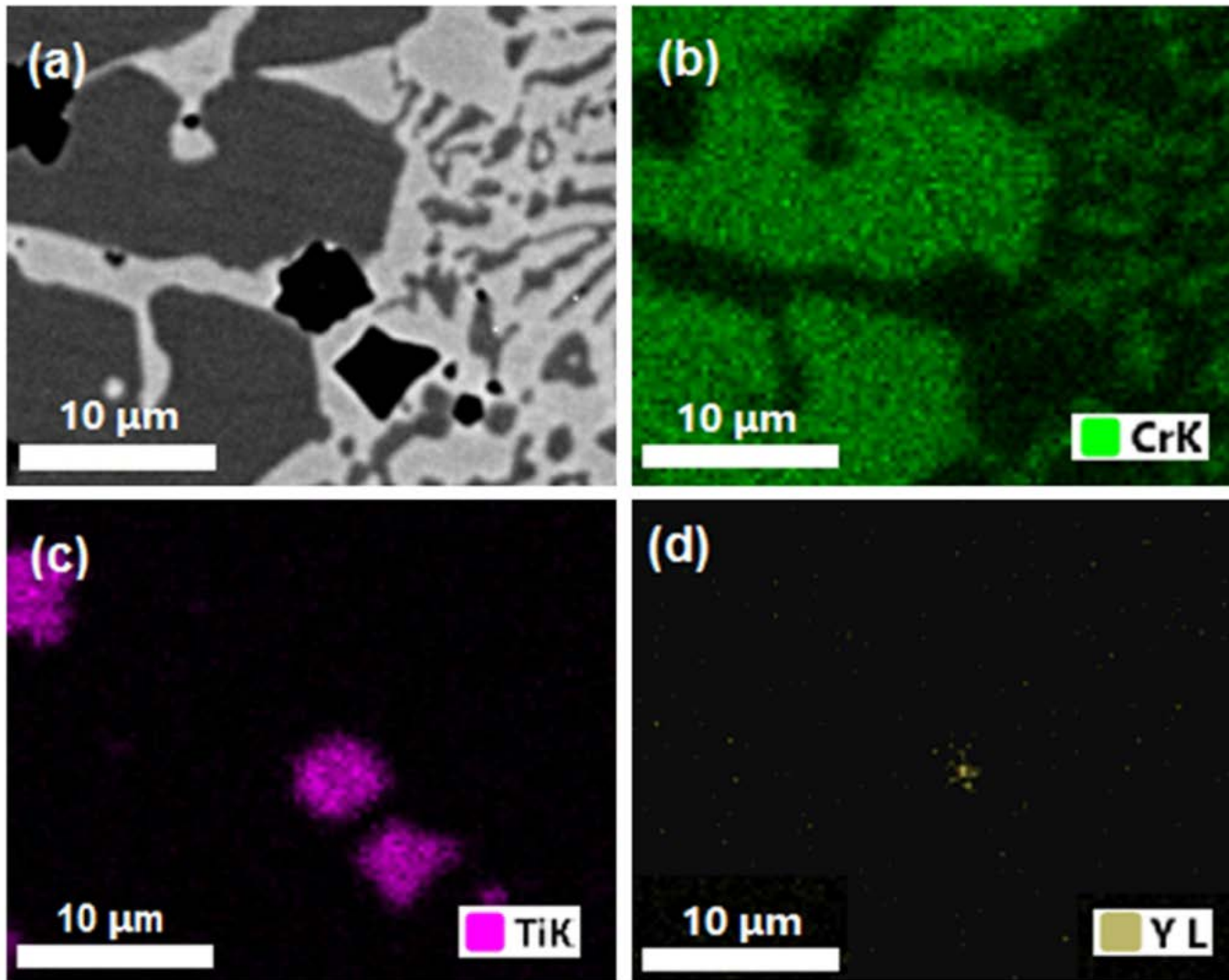


Fig. 11

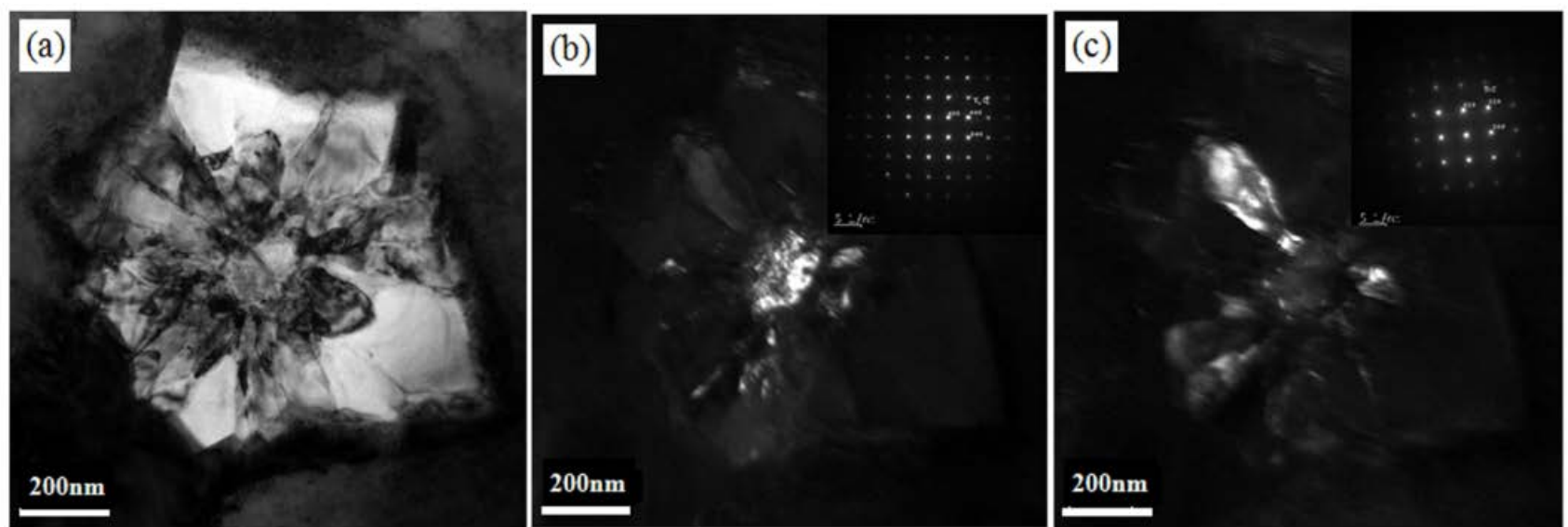


Fig. 12